



# Experimental study on the gas-stripping chamber of an E//B neutral particle analyzer

Long Ma<sup>1</sup> · De-Hao Xie<sup>1</sup> · Yan-Xi Wang<sup>1</sup> · Shuo Wang<sup>1</sup> · Ji-Feng Han<sup>1</sup> · Wei-Ping Lin<sup>1</sup> · Jian-Li Liu<sup>2</sup> · Xing-Quan Liu<sup>1</sup> · Yu-Guo Liu<sup>2</sup> · Xiao-Bing Luo<sup>1</sup> · Yuan Luo<sup>3</sup> · Guo-Feng Qu<sup>1</sup> · Yu-Fan Qu<sup>3</sup> · Pei-Pei Ren<sup>1</sup> · Roy Wada<sup>4</sup> · Lin-Ge Zang<sup>3</sup> · Jing-Jun Zhu<sup>1</sup>

Received: 22 August 2023 / Revised: 3 May 2024 / Accepted: 8 May 2024 / Published online: 12 October 2024

© The Author(s), under exclusive licence to China Science Publishing & Media Ltd. (Science Press), Shanghai Institute of Applied Physics, the Chinese Academy of Sciences, Chinese Nuclear Society 2024

## Abstract

Stripping units take a key role in the neutral particle analyzer (NPA). A renovated gas-stripping unit was constructed for the newly designed E//B NPA. Using H<sub>2</sub> as the working gas, we measured the gas inlet pressure ( $P_0$ ) and vacuum chamber pressure ( $P_3$ ). The pressure distribution inside the gas-stripping room was calculated with Ansys Fluent, using the measured  $P_0$  and  $P_3$  as boundary conditions. The stripping efficiency of the stripping unit was then simulated utilizing the Geant4 Monte Carlo code for the H and D particles. The pressure  $P_0 = 40$  Pa, which is one-sixth of what found in the previous design and corresponds to a thickness of  $1.27 \times 10^{17}$  atoms/cm<sup>2</sup>, was obtained as the optimum working pressure for the upgraded stripping unit. An 50 kV electron cyclotron resonance (ECR) ion source platform was designed and constructed for E//B NPA calibration, and its performance has been measured. Using the ECR ion source platform, we measured the efficiency of the stripping unit through an inverse experiment with proton beams. We compared the current ratios of measurements with and without H<sub>2</sub> gas to Geant4 simulation results. We found adequate agreement between the overall trends of the experiment and the simulation. The significant deviation for incident energies below 20 keV may result from the scattering effects of low-energy protons, leading to reduced accuracy in single-scattering physics in Geant4 simulations. Applying the scattering corrections observed in the reverse experiments obtains more accurate stripping efficiencies for H and D atoms in the energy range of 20–200 keV and the global efficiency with the maximum values of 95.0% for H atoms and 78.9% for D atoms at 200 keV.

**Keywords** NPA · Gas-stripping · ECR ion source · Stripping efficiency · Geant4

This work was supported by the National MCF Energy R & D Program of China (MOST 2018YFE0310200), in part by the National Natural Science Foundation of China (Nos. 11705242, 11805138, and 12175156), and in part by the Fundamental Research Funds for the Central Universities (Nos. YJ201820, YJ201954) in China.

✉ Wei-Ping Lin  
linwp1204@scu.edu.cn

✉ Jing-Jun Zhu  
zhujingjun@scu.edu.cn

<sup>1</sup> Key Laboratory of Radiation Physics and Technology of the Ministry of Education, Institute of Nuclear Science and Technology, Sichuan University, Chengdu 610064, China

## 1 Introduction

A tokamak is a magnetic-confinement fusion device used in controllable fusion experiments. The interaction between the shear Alfvén wave and energetic particles plays a crucial role in the high-temperature plasma confinement and steady-state operation of tokamaks [1–11]. Several diagnostic devices

<sup>2</sup> Institute of Modern Physics, Chinese Academy of Sciences, Lanzhou 730000, China

<sup>3</sup> Southwestern Institute of Physics, Chengdu 610218, China

<sup>4</sup> Cyclotron Institute, Texas A & M University, College Station, TX 77843, USA

have been developed to study fusion plasma and the energetic particles on tokamaks, such as microwave diagnostics [12–14], soft X-ray diagnostics [15–17], neutron diagnostics [18–25], the visible/infrared camera [26–29], and the neutral particle analyzer (NPA) [30–37]. NPA is of great importance in providing energy spectra, which are key information for the frontier physics of energetic particles [4–6, 9, 38–40]. The bulk ion temperature, isotopic ratio, and fast-ion distribution of the plasma were obtained by measuring the charge exchange of neutral particles escaping from the plasma.

Since the first NPA was developed in 1960 [30], several NPAs have been designed and constructed worldwide [31–37, 41–50]. For example, the compact NPA (CNPA) [34] developed for the Wendelstein 7-AS stellarator offers the advantage of simultaneous analysis for hydrogen (0.8–80 keV) and deuterium (0.8–40 keV) with a more compact structure (size: 169 mm × 302 mm × 326 mm, weight: 42.5 kg). The NPA system on the international thermonuclear experimental reactor (ITER) includes a high-energy NPA to measure the D and T atoms within the energy ranges of 0.11–1.4 MeV and 0.16–2.2 MeV, respectively, and a low-energy NPA for the thermal energy range from 10 to 200 keV for all hydrogen isotopes [32, 48].

Typically, NPA comprises three main components: stripping, analyzing, and detection units. A stripping unit reionizes neutral particles via charge exchange reactions with the stripping material. The reionized particle energy and/or mass was identified by the magnetic and/or electric fields and recorded by the detecting unit. Various types of ion detectors [51], including micro-channel plates [35, 52–55], channel electron multipliers [34, 37, 56], CsI [31, 32, 50, 57, 58], LYSO scintillators [49, 59, 60], and diamond-like detectors [61, 62], are employed for the detecting unit of an NPA. The stripping material can be a stripping foil or gas. When using a solid foil as the stripping material in the NPA for low-energy neutrals, an additional accelerating or focusing voltage is often required for secondary ions [31, 32, 34]. Carbon foil with a thickness of 100 Å is commonly used as the stripping foil. In contrast, a gas chamber requires a differential pumping system when using a stripping gas. Typically, an integrated target with a thickness of the order of  $10^{16}$  atoms/cm<sup>2</sup> for H<sub>2</sub> gas is used in the joint European torus (JET) NPA [44] and  $10^{15}$  atoms/cm<sup>2</sup> for He gas in the E//B NPA on TFTR [35]. This low-pressure operation is necessary to sustain a high vacuum level in the tokamak, resulting in low stripping efficiency.

A new NPA with parallel electric and magnetic fields (E//B) for studying the frontier physics of energetic particles is currently under development [63, 64]. A gas-stripping room filled with H<sub>2</sub> as the working gas was adopted as the stripping unit in the E//B NPA. In a previous work Ref. [64], we presented the pressure distributions inside the stripping

room simulated by Ansys Fluent [65, 66] and Molflow+ [67]. The stripping efficiencies of H and D atoms passing through the stripping unit were then calculated using Geant4 [68, 69] simulation code. This study presents an experimental investigation of pressure distributions inside an upgraded stripping room, optimizing the initial design from [64, 70], and the ion beam tests of the stripping unit on a newly constructed 50 kV electron cyclotron resonance (ECR) ion source platform at Sichuan university.

The remainder of this paper is organized as follows. An experimental investigation of the pressure distribution inside the stripping room is presented in Sect. 2. Section 3 covers the newly constructed 50 kV ECR ion source platform and its performance. The ion beam tests of the stripping unit are detailed in Sect. 4. A brief summary is provided in Sect. 5.

## 2 Pressure distribution and stripping efficiency of the stripping unit

Our previous study presented a prototype design of the gas-stripping chamber [64, 70], where a stripping room with a length of 54 mm and two differential pipes with inner diameters of 4 mm was designed. The pressure distribution inside the stripping room was calculated using Ansys Fluent [65] and Molflow+ [67], assuming a constant pumping speed for the outlet surface. The stripping unit, constructed from a prototype design, exhibited reduced molecular pump speed when the pressure exceeded a certain value, resulting in higher vacuum chamber pressure compared to Ansys Fluent and Molflow+ calculations. Therefore, the stripping room structure was modified to reduce pressure in the vacuum chamber. An upgraded stripping room with a length of 84 mm and a differential pipes' inner diameter of 2 mm was constructed for the stripping unit. Figure 1 shows a cross-sectional view of the upgraded gas-stripping chamber.

Figure 2 shows a photograph of the upgraded stripping unit. A Faraday cup (FC) located in the downstream vacuum chamber was constructed, along with a stripping unit, to measure the incident beam current. A needle valve and an

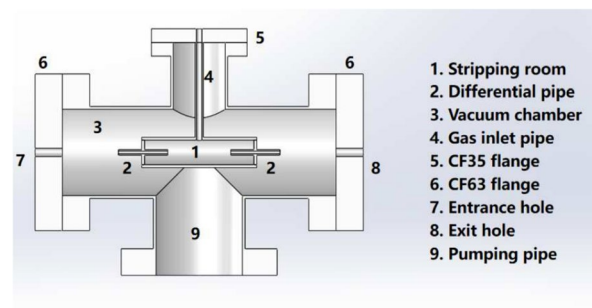


Fig. 1 Cross-sectional view of the upgraded gas-stripping chamber



**Fig. 2** Photograph of the upgraded stripping unit. (Color figure online)

electromagnetic valve controlled by a proportional–integral–derivative (PID) controller were connected to the gas inlet flange to stabilize the H<sub>2</sub> gas flow. Two diaphragm vacuum gauges, Pfeiffer CMR362 and CMR365, were used to measure the pressures of the gas inlet ( $P_0$ ) and vacuum chamber ( $P_3$ ), respectively. The pressure distribution inside the stripping room was obtained by applying the two measured pressures as the boundary conditions in Ansys Fluent.

By utilizing the experimentally measured  $P_3$  value in the Ansys Fluent calculations, a more accurate prediction of the pressure distribution inside the stripping room was obtained. Figure 3 shows a typical two-dimensional (2D) pressure distribution of  $P_0 = 40$  Pa on the central plane ( $Z = 0$  mm) of the stripping room in (a) and the pressure distribution along the incident neutral particles’ path ( $Y = 0$  mm and

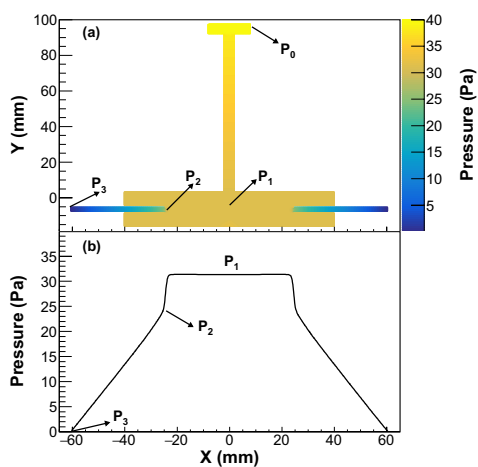


**Fig. 3** **a** 2D pressure distribution of  $P_0 = 40$  Pa in the central plane ( $Z = 0$  mm) of the stripping room. **b** Pressure distribution along the path of the incident neutral particles ( $Y = 0$  mm and  $Z = 0$  mm) in the stripping room for  $P_0 = 40$  Pa. The inlet pressure ( $P_0$ ), the pressures of the center of the stripping room ( $P_1$ ), the inner end of the differential pipes ( $P_2$ ), and the vacuum chamber ( $P_3$ ) are indicated in the figure. (Color figure online)

$Z = 0$  mm) in the stripping room for  $P_0 = 40$  Pa in (b). With a reduction in the differential pipes’ inner diameter in the upgraded stripping unit, a higher pressure inside the stripping room is expected for a given  $P_0$ . As shown in Fig. 3b, a constant pressure of approximately 31 Pa is applied in the center of the stripping room, which is more than three times that of the previous design [64]. The linearly decreasing pressures inside the differential pipes were also obtained.

The pressures of the center of the stripping room ( $P_1$ ) and the inner end of the differential pipes ( $P_2$ ) were extracted and are shown together with  $P_3$  as a function of the inlet pressure  $P_0$  in Fig. 4. A linearly increasing trend of  $P_1$  is observed as the inlet pressure  $P_0$  increases, whereas slightly nonlinear changes in  $P_2$  and  $P_3$  are observed. This may result from variations in the pumping speed for different  $P_0$  values, leading to nonlinear changes in  $P_2$  and  $P_3$ .

Geant4 [68, 69] Monte Carlo was applied to simulate the global stripping efficiency ( $R \times f_{+1}$ , where  $R$  represents the transmission rate of the stripping room and  $f_{+1}$  is the fraction of the +1 charge state at the exit hole of the stripping chamber) of an earlier version of the stripping unit, and an optimum  $P_0$  pressure of 240 Pa was obtained in our previous work [64, 70]. In the simulation, the charge exchange cross sections of the ORNL-recommended dataset [71] were employed, including the electron capture and loss cross sections of  $H^0$ , the electron capture cross sections of  $H^+$ , and the loss cross sections of  $H^-$ . Taking the charge exchange cross sections at a given energy allows for obtaining the stripping efficiency from a simple equation without scattering corrections, as shown in Eq. (1) in [64]. The  $R \times f_{+1}$  values were obtained by modifying the structure and pressure distribution in the code to match the upgraded stripping unit. Figure 5 shows  $R \times f_{+1}$  as a function of the gas inlet pressure  $P_0$  for H and D atoms with incident energies 20 keV, 100 keV, and 200 keV in (a), (b),

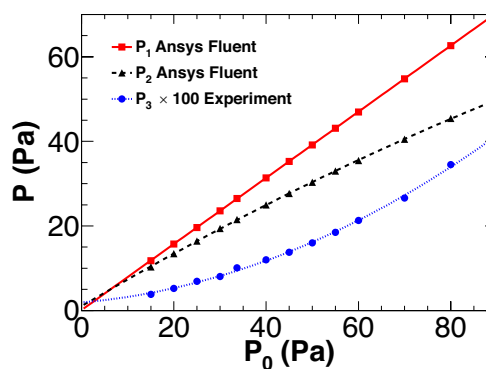


**Fig. 4**  $P_1$  (solid squares),  $P_2$  (solid triangles), and  $P_3$  (solid circles) as a function of  $P_0$ . The solid curve is the linear fit of  $P_1$ . Dashed and dotted curves are the second-order polynomial fit of  $P_2$  and  $P_3$ , respectively.  $P_3$  is multiplied by a factor of 100 for easier comparison. (Color figure online)

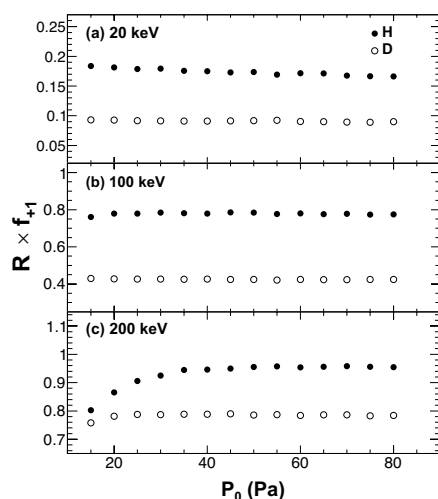


**Fig. 5** Global efficiency  $R \times f_{+1}$  as a function of the gas inlet pressure  $P_0$  for incident energies 20 keV (a), 100 keV (b), 200 keV (c). The solid and open circles represent H and D, respectively

and (c), respectively. As the length of the stripping room increased, the thickness of the stripping gas increased in the upgraded stripping unit. Thus, a lower  $P_0$  value was required to achieve the same global stripping efficiency in the upgraded stripping unit. One can see from Fig. 5, the global efficiency increases with the gas inlet pressure  $P_0$  and reaches a maximum value of approximately 40 Pa for the maximum designed energy (200 keV) in the upgraded stripping unit. The optimum working pressure for the upgraded stripping unit was determined to be  $P_0 = 40$  Pa, five times lower than in the previous design [64], corresponding to a thickness of  $1.27 \times 10^{17}$  atoms/cm<sup>2</sup>.

### 3 The 50 kV ECR ion source platform

A new 50 kV ECR ion source platform with a compact permanent-magnet ECR ion source and a 30° dipole magnet was designed and constructed at Sichuan University to calibrate the E//B NPA. In general, the ion source platform consists of an ECR ion source, a dipole magnet, an FC, and vacuum and water-cooling systems. Figure 6 shows a photograph of the 50 kV ECR ion source platform.

As shown in Fig. 7, a more compact and concise 2.45 GHz single-charge-state ECR ion source, modified from [72], was developed for the new 50 kV ECR ion source platform. The outer diameter of the source body was 50 mm. The magnetic field was produced by a single NdFeB permanent-magnet ring. A plasma chamber of diameter 30 mm and length 30 mm was designed for the ion source. The suppressor and shield electrodes described in [72] were removed from the ion source. The diameters of the plasma and extraction apertures were reduced to 3 mm and 5 mm, respectively.



**Fig. 6** Photograph of the 50 kV ECR ion source platform. (Color figure online)

The newly designed spherical antenna head, which increased the plasma density in the chamber by approximately 10%, was used for the ion source. The length of the ceramic insulator tube was extended to 120 mm to sustain the 50 kV extraction voltage. The high-voltage power supply exhibited a 0.1% voltage drift over time and temperature. The microwave power source, placed on a high-voltage platform, was coupled to the plasma chamber via a coaxial cable and antenna. An isolation transformer rated for up to 80 kV and 1 kVA supplied power to the microwave generator. A needle valve with a leakage rate of  $10^{-9}$  Pa · L · s<sup>-1</sup> controlled the inlet flow of the working gas. The energy spread that was caused by the plasma instabilities in the extracted beam was measured by a retarding field energy analyzer revealed a maximum spread of less than 5 eV.

A dipole magnet with a deflection angle of 30°, deflection radius of 250 mm, gap of 40 mm, and width of 70 mm was installed to analyze 50 keV He<sup>+</sup> particles from the ECR ion source. As shown in the schematic of the 50 kV ECR ion source platform in Fig. 8, the ECR ion source and the dipole magnet were connected to a vacuum chamber (A). The other vacuum chamber (B) was located downstream of the dipole magnet. Two identical molecular pumps with pumping speeds of 700 L/s (N<sub>2</sub>) were mounted on the two chambers

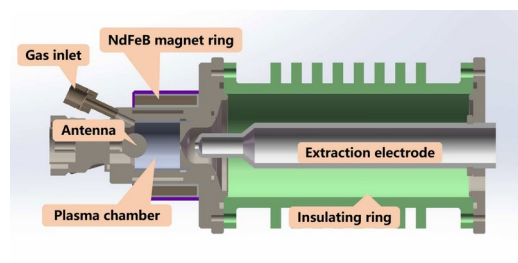


**Fig. 7** Structure drawing of the ECR ion source. (Color figure online)

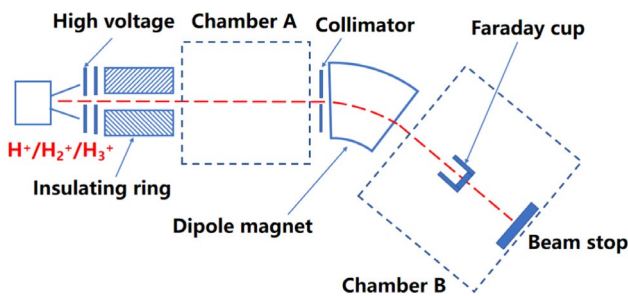


Fig. 8 Schematic diagram of the ECR ion source platform

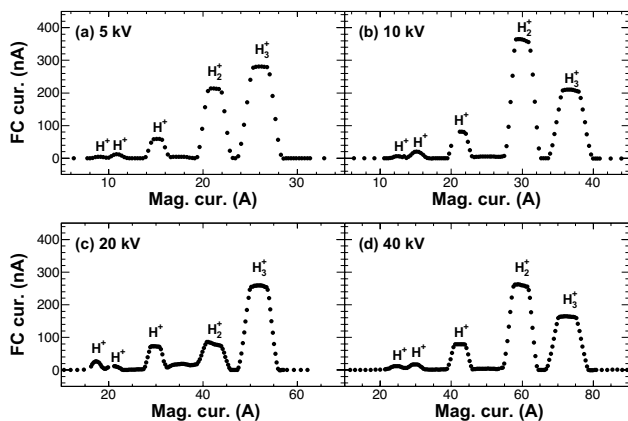


Fig. 9 Typical beam current as a function of the magnetic current for the extraction voltage 5 keV (a), 10 keV (b), 20 keV (c), and 40 keV (d)

to maintain fine vacuum conditions. A collimator of diameter 5 mm was installed between Chamber A and the dipole magnet to reduce the beam spot after the dipole magnet. Using this collimator, a typical beam spot with a diameter of less than 15 mm was obtained for proton beams with an incident energy of 20 keV at the terminal flange. An FC with an entrance diameter of 2 cm was mounted in Chamber B to measure the beam intensity. The platform was equipped with a temperature-controlled deionized water-cooling system for the ion source and the dipole magnet.

The performance of the 50 kV ECR ion source platform was measured using hydrogen gas with 99.999% purity as the working gas. The beam current was measured using the FC in vacuum chamber B. The FC suppressor electrode was biased toward  $-300$  V to suppress the secondary electrons. Figure 9 shows the typical beam current as a function of the magnetic current for extraction voltages of 5 keV, 10 keV, 20 keV, and 40 keV in (a), (b), (c), and (d), respectively. The three large peaks from right to left are  $H_3^+$ ,  $H_2^+$ , and  $H^+$ . The two small peaks on the low-magnetic-current side are the breakup  $H^+$  events from  $H_3^+$  (left) and  $H_2^+$  (right). A small peak is observed between the largest  $H^+$  and  $H_2^+$  peaks at an extraction voltage of 20 keV, corresponding to the breakup

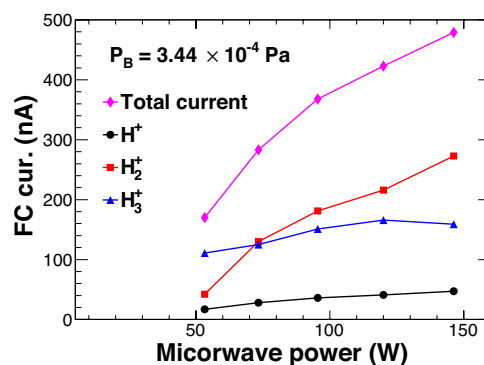


Fig. 10 Total,  $H^+$ ,  $H_2^+$ , and  $H_3^+$  currents as a function of the microwave power

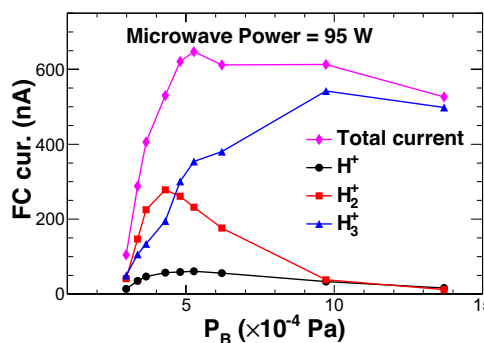


Fig. 11 Total current,  $H^+$ ,  $H_2^+$ , and  $H_3^+$  beam intensities as functions of  $P_B$ . (Color figure online)

of  $H_2^+$  from  $H_3^+$ . Rather small yields of breakup  $H_2^+$  were found at other extraction voltages. Notably, the gas inlet flow changed for the above four extraction voltages, leading to a difference in the charged-particle yield shown in Fig. 9. The charged-particle composition should be further optimized for actual applications.

The charged-particle intensity dependence on the microwave power was measured at a constant gas inlet flow and an extraction voltage of 5 keV. The gas inlet flow was monitored using the pressure measured in Chamber B. A constant pressure of  $P_B = 3.44 \times 10^{-4}$  Pa was maintained throughout the measurements. The breakup of charged particles was ignored in this analysis because of low production yields. Figure 10 shows the total,  $H^+$ ,  $H_2^+$ , and  $H_3^+$  currents as functions of the microwave power. The total current was calculated by summing currents  $H^+$ ,  $H_2^+$ , and  $H_3^+$ . Figure 10 shows that the total current increased dramatically when the microwave power rose from 53 to 146 W, which is consistent with the results in [72]. As microwave power increased, the fractions of  $H^+$  and  $H_2^+$  rose, while  $H_3^+$  decreased at powers above 120 W. This may be due to the increase in the electron

density with higher microwave power [73], which produces more  $H_2^+$ .

The dependence of the charged-particle intensity on the gas inlet flow was measured at a fixed microwave power of 95 W and an extraction voltage of 5 keV. Figure 11 shows the total,  $H^+$ ,  $H_2^+$ , and  $H_3^+$  currents as functions of  $P_B$ . The total current rapidly increased, peaking at  $P_B = 5.27 \times 10^{-4}$  Pa and then gradually decreased as  $P_B$  increased further. The  $H^+$  intensity increased smoothly with  $P_B$ , peaking at the same  $P_B$  value as the total current. The  $H_2^+$  intensity peaked at a lower pressure of  $P_B = 3.7 \times 10^{-4}$  Pa, while  $H_3^+$  dominated at  $P_B$  above  $5 \times 10^{-4}$  Pa.

A  $H_3^+$  beam intensity comparable to that of  $H_2^+$  was observed for all microwave powers, as shown in Fig. 10. At higher gas inlet flow rates, the  $H_3^+$  fraction exceeded (more than 90 %), as shown in Fig. 11. High  $H_3^+$  fractions are reported in pulse-type ECR ion sources [74] but not in DC-mode ECR ion sources. Studies show that higher working gas pressure and lower microwave power in ECR ion sources increase  $H_3^+$  production [74, 75]. The extremely high  $H_3^+$  ion fraction in our 50 kV ECR ion source platform may result from the small discharge chamber and extraction hole, leading to higher pressure. This is significant for intense  $H_3^+$ -beam applications.

#### 4 The experimental test of the gas-stripping unit

Calibration of the gas-stripping unit is crucial for the NPA. Direct verification of simulated results in the laboratory is challenging owing to the difficulty in handling neutral particles for precise measurements. However, because the stripping cross sections from neutrals to ions and the captured cross sections from ions to neutrals are comparable at a given energy [64], verification can be performed using ion beams in a reverse scenario.

Reverse experiments were conducted using the 50 kV ECR ion source platform. Figure 12 shows the schematic

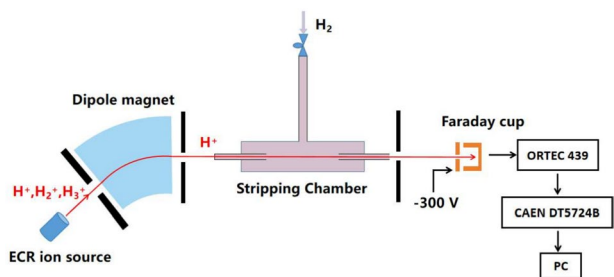


**Fig. 12** Schematic diagram of the experimental setup of the gas-stripping unit on the 50 kV ECR ion source platform. (Color figure online)

of the gas-stripping unit experimental setup on this platform. Proton beams with energies of 5 keV, 10 keV, 20 keV, 30 keV, and 40 keV were delivered to the gas-stripping unit. After charge exchange processes in an  $H_2$ -filled stripping room, the total current of the remaining charged particles was measured using the FC located in the downstream chamber. A digital current integrator (ORTEC 439) measured the current of the charged particles in the FC, with the output pulse recorded by a CAEN DT5724B digitizer. The beam current without  $H_2$  gas was measured before and after each experiment as a reference. Experiments were conducted at gas inlet pressures of  $P_0 = 20$  Pa, 30 Pa, and 40 Pa for each incident proton energy.

In the experiment, each ORTEC 439 pulse corresponded to  $10^{-10}$  C. An FC current was recorded for each measurement. Figure 13 shows the FC current as a function of the recording time for 20 keV incident protons. The solid circles, solid down triangles, and open squares represent the vacuum conditions in the stripping room at the beginning, middle, and end of the 20 keV proton measurements, respectively. The solid squares, solid triangles, and open circles represent measurements with filled  $H_2$  gas pressures of  $P_0 = 40$  Pa, 30 Pa, and 20 Pa, respectively. The solid lines indicate linear fits. A slight decreasing trend of less than 0.5% over the recording period for the three vacuum measurements suggests the long-term stability of the ECR ion source. Measurements under vacuum conditions before and after those with  $H_2$  gas serve as a reliable reference for the beam intensity of those with  $H_2$  gas.

The current ratios for measurements with and without (vacuum)  $H_2$  gas were obtained from the FC currents ratios. The linear fit from vacuum measurements was used to extrapolate the beam currents for each  $H_2$  gas measurement.

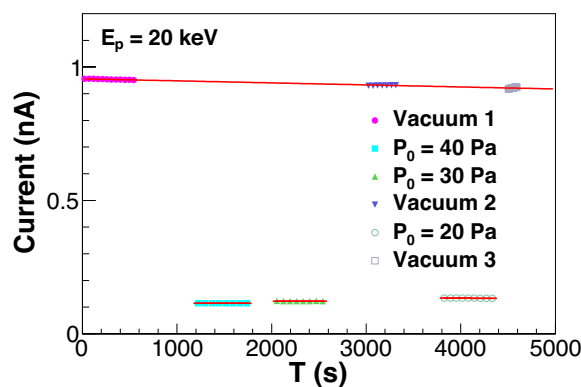


**Fig. 13** FC current as a function of the recording time for 20 keV incident protons. Solid circles, solid down triangles, and open squares correspond to the vacuum condition in the stripping room at the beginning, middle, and end of 20 keV proton measurements; solid squares, solid up triangles, and open circles represent measurements with filled  $H_2$  gas pressure of  $P_0 = 40$  Pa, 30 Pa, and 20 Pa, respectively. Solid lines represent linear fits. (Color figure online)

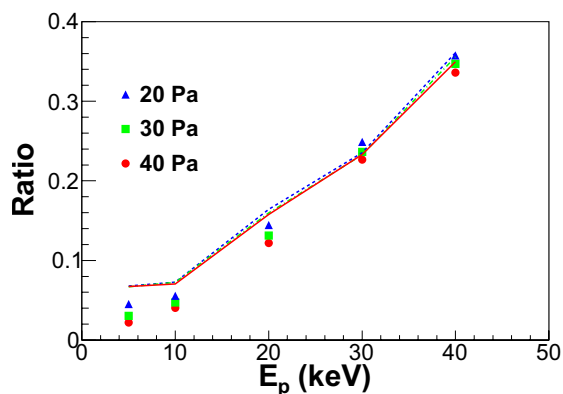


**Fig. 14** Current ratio of the measurements between with and without (vacuum) H<sub>2</sub> gas as a function of the proton energy for  $P_0 = 20$  Pa (solid triangles), 30 Pa (solid squares), and 40 Pa (solid circles). The dotted, dashed, and solid curves are the Geant4 simulations for  $P_0 = 20$  Pa, 30 Pa, and 40 Pa, respectively. (Color figure online)

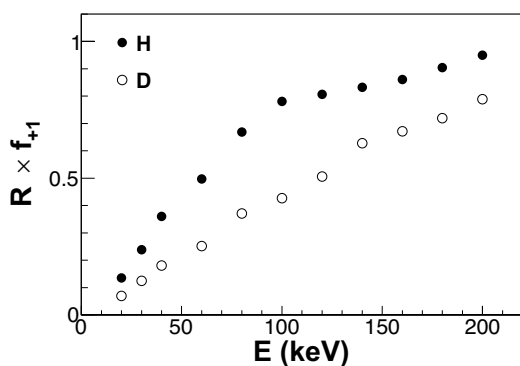


**Fig. 15** Global efficiency  $R \times f_{+1}$  as a function of the incident energy at  $P_0 = 40$  Pa. The solid and open circles represent H and D atoms, respectively

Figure 14 shows the current ratio as a function of the proton energy ( $E_p$ ) for  $P_0 = 20$  Pa (solid triangles), 30 Pa (solid squares), and 40 Pa (solid circles); Geant4 simulations with proton beams are presented for comparison. The ratio rapidly increased as  $E_p$  increased at  $E_p > 10$  keV and showed a flat trend at  $E_p \leq 10$  keV. This trend is consistent with the electron removal cross section ( $\sigma_{0,1}$ ) shown in [71]. This was confirmed by a Geant4 simulation, in which the same overall trend was obtained. One can observe from Fig. 14, noticeable deviations between the simulation and experiment for the proton energy  $E_p \leq 20$  keV. Geant4 simulations yielded nearly identical results for a given  $E_p$  across three different  $P_0$  values. This consistency may arise from accuracy limitations in single-scattering physics at energies below 20 keV, leading to significant deviations in the simulations. The E//B NPA was designed for an energy range of 20–200 keV, where scattering effects for low-energy particles are small for incident energies above 30 keV.

The scattering effects from reverse experiments for low-energy ( $E \leq 30$  keV) protons were used to adjust the stripping efficiency from Geant4 simulations, as shown in Fig. 15. The global stripping efficiencies for H and D gradually increased with energy from 20 to 200 keV, reaching a maximum value of 95.0% for H atoms and 78.9% for D atoms at 200 keV. These results indicate that the upgraded stripping room has excellent stripping capability for H and D atoms within the energy range of 20–200 keV at  $P_0 = 40$  Pa.

### 5 Summary

An upgraded stripping unit of the newly designed E//B NPA was constructed. We measured the dependence of the vacuum chamber pressure ( $P_3$ ) on the gas inlet pressure ( $P_0$ ) and used these measurements as boundary conditions in Ansys Fluent to obtain the internal pressure distributions. The stripping unit efficiency was simulated using the Geant4 Monte Carlo code. Modifying the stripping room length from 54 to 84 mm and the inner radius of the differential pipes from 4 to 2 mm resulted in a central pressure ( $P_1$ ) over three times higher than that in the previous design. An optimal pressure of  $P_0 = 40$  Pa was achieved, which is reduced to one-sixth of the previous value and corresponds to a thickness of  $1.27 \times 10^{17}$  atoms/cm<sup>2</sup>.

A 50 kV ECR ion source platform was designed and constructed to calibrate the E//B NPA at Sichuan University. A more compact 2.45 GHz single-charge ECR ion source, capable of providing H<sup>+</sup>, H<sub>2</sub><sup>+</sup>, and H<sub>3</sub><sup>+</sup> beams at energies below 50 keV was developed for this platform. Performance measurements with H<sub>2</sub> as the working gas offer valuable insights for future applications.

The stripping efficiency of the stripping unit was investigated in the reverse scenario using the 50 kV ECR ion source platform. Instead of using neutral beams, proton beams with energies of 5 keV, 10 keV, 20 keV, 30 keV, and 40 keV were delivered to the stripping unit, which was filled with H<sub>2</sub> gas at inlet pressures of  $P_0 = 20$  Pa, 30 Pa, and 40 Pa. The beam current was measured by an FC in the vacuum chamber located downstream of the stripping unit. The current ratios of the measurements with and without H<sub>2</sub> gas were compared with those of Geant4 simulations. The experiment and simulation exhibited good overall agreement. The significant deviation at incident energies below 20 keV may stem from the differences between the scattering effect and the single-scattering physics of low-energy protons in Geant4 simulations. Considering this scattering effect, more accurate stripping efficiencies were obtained, with maximum global efficiencies of 95.0% for H atoms and 78.9% for D atoms at 200 keV.

**Author contributions** All authors contributed to the study conception and design. Material preparation, data collection, and analysis were performed by Long Ma, De-Hao Xie, Yan-Xi Wang, Wei-Ping Lin. The first draft of the manuscript was written by Long Ma, and all authors commented on previous versions of the manuscript. All authors read and approved the final manuscript.

**Data availability** The data that support the findings of this study are openly available in Science Data Bank at <https://cstr.cn/31253.11.sciencedb.j00186.00227> and <https://www.doi.org/10.57760/sciencedb.j00186.00227>.

## Declarations

**Conflict of interest** The authors declare that they have no conflict of interest.

## References

1. Y. Liu, X.T. Ding, Q.W. Yang et al., Recent advances in the HL-2A tokamak experiments. *Nucl. Fusion* **45**, S239 (2005). <https://doi.org/10.1088/0029-5515/45/10/S19>
2. Q.W. Yang, Y. Liu, X.T. Ding et al., Overview of HL-2A experiment results. *Nucl. Fusion* **47**, S635 (2007). <https://doi.org/10.1088/0029-5515/47/10/S12>
3. X.Z. Gong, B.N. Wan, J.G. Li et al., Realization of minute-long steady-state H-mode discharges on EAST. *Plasma Sci. Technol* **19**, 032001 (2017). <https://doi.org/10.1088/2058-6272/19/3/032001>
4. L. Chen, F. Zonca, Physics of Alfvén waves and energetic particles in burning plasmas. *Rev. Mod. Phys.* **88**, 015008 (2016). <https://doi.org/10.1103/RevModPhys.88.015008>
5. X.T. Ding, W. Chen, Review of the experiments for energetic particle physics on HL-2A. *Plasma Sci. Technol* **20**, 97 (2018). <https://doi.org/10.1088/2058-6272/aad27a>
6. N.N. Gorelenkov, S.D. Pinches, K. Toi, Energetic particle physics in fusion research in preparation for burning plasma experiments. *Nucl. Fusion* **54**, 125001 (2014). <https://doi.org/10.1088/0029-5515/54/12/125001>
7. P.W. Shi, X.L. Zhu, A.S. Liang et al., Mitigation of long-lived modes by lower hybrid wave on the HL-2A tokamak. *Nucl. Fusion* **62**, 106009 (2022). <https://doi.org/10.1088/1741-4326/ac8691>
8. L.M. Yu, W. Chen, X.Q. Ji et al., Observation of multiple broadband Alfvénic chirping modes in HL-2A NBI plasmas. *Chin. Phys. Lett.* **38**, 055202 (2021). <https://doi.org/10.1088/0256-307x/38/5/055202>
9. P.W. Shi, W. Chen, X.R. Duan, Energetic particle physics on the HL-2A tokamak: a review. *Chin. Phys. Lett.* **38**, 035202 (2021). <https://doi.org/10.1088/0256-307x/38/3/035202>
10. S.T. Wu, The EAST team, an overview of the EAST project. *Fusion Eng. Des.* **82**, 463 (2007). <https://doi.org/10.1016/j.fusengdes.2007.03.012>
11. Y.X. Wan, J.G. Li, Y. Liu et al., Overview of the present progress and activities on the CFETR. *Nucl. Fusion* **57**, 102009 (2017). <https://doi.org/10.1088/1741-4326/aa686a>
12. H.L. Zhao, T.F. Zhou, Y. Liu et al., Upgrade of the ECE diagnostic on EAST. *Rev. Sci. Instrum.* **89**, 10H111 (2018). <https://doi.org/10.1063/1.5035452>
13. Z.J. Yang, Y. Xiao, X.D. Ma et al., The design of a correlation electron cyclotron emission system on J-TEXT. *Rev. Sci. Instrum.* **86**, 043501 (2015). <https://doi.org/10.1063/1.4917271>
14. M. Jiang, Z.B. Shi, S. Che et al., Development of electron cyclotron emission imaging system on the HL-2A tokamak. *Rev. Sci. Instrum.* **84**, 113501 (2013). <https://doi.org/10.1063/1.4828671>
15. K.Y. Chen, L.Q. Xu, L.Q. Hu et al., 2-D soft x-ray arrays in the EAST. *Rev. Sci. Instrum.* **87**, 063504 (2016). <https://doi.org/10.1063/1.4953837>
16. Y.L. Li, G.S. Xu, K. Tritz et al., Edge multi-energy soft x-ray diagnostic in experimental advanced superconducting tokamak. *Rev. Sci. Instrum.* **86**, 123512 (2015). <https://doi.org/10.1063/1.4938155>
17. B. Alper, S. Dillon, A.W. Edwards et al., The JET soft x-ray diagnostic systems. *Rev. Sci. Instrum.* **68**, 778 (1997). <https://doi.org/10.1063/1.1147645>
18. L. Bertalot, R. Barnsley, M.F. Direz et al., Fusion neutron diagnostics on ITER tokamak. *J. Instrum.* **7**, C04012 (2012). <https://doi.org/10.1088/1748-0221/7/04/C04012>
19. J. Cao, C.Y. Jiang, H.R. Cao et al., Experimental validation of a Tokamak neutron spectrometer based on Bonner spheres. *Chin. Phys. C* **39**, 086001 (2015). <https://doi.org/10.1088/1674-1137/39/8/086001>
20. J. Cao, C.Y. Jiang, Q.W. Yang et al., Verification of a fusion neutron diagnostic Bonner sphere spectrometer on measurement of a  $^{241}\text{Am}$ -Be neutron source. *Nucl. Sci. Tech.* **27**, 128 (2016). <https://doi.org/10.1007/s41365-016-0126-2>
21. B.W. Zheng, C.Y. Jiang, Z.H. Liu et al., Correction and verification of HL-2A Tokamak Bonner sphere spectrometer in monoenergetic neutron fields from 100 keV to 5 MeV. *Nucl. Sci. Tech.* **30**, 159 (2019). <https://doi.org/10.1007/s41365-019-0689-9>
22. B.W. Zheng, W. Zhang, T.Y. Wu et al., Development of the real-time double-ring fusion neutron time-of-flight spectrometer system at HL-2M. *Nucl. Sci. Tech.* **30**, 175 (2019). <https://doi.org/10.1007/s41365-019-0702-3>
23. X.F. Jiang, J. Cao, C.Y. Jiang et al., Tokamak fusion neutron spectrometer based on PXI bus. *Nucl. Sci. Tech.* **25**, 4 (2014). <https://doi.org/10.13538/j.1001-8042/nst.25.040401>
24. R.J. Zhu, X. Zhou, Z.H. Liu et al., High-precision and wide-range real-time neutron flux monitor system through multipoint linear calibration. *Nucl. Sci. Tech.* **31**, 94 (2020). <https://doi.org/10.1007/s41365-020-00798-3>
25. W.D. Wang, H.R. Gao, J. Cao et al., A study of beryllium moderator thickness for a fission chamber with fast neutron measurements. *Nucl. Sci. Tech.* **28**, 129 (2017). <https://doi.org/10.1007/s41365-017-0283-y>
26. C.J. Boswell, J.L. Terry, B. Lipschultz et al., Applications of visible CCD cameras on the Alcator C-Mod tokamak. *Rev. Sci. Instrum.* **72**, 935 (2001). <https://doi.org/10.1063/1.1321010>
27. S.B. Shu, C.M. Yu, C. Liu et al., Improved plasma position detection method in EAST Tokamak using fast CCD camera. *Nucl. Sci. Tech.* **30**, 24 (2019). <https://doi.org/10.1007/s41365-019-0549-7>
28. Z.X. Cui, X. Li, S.B. Shu et al., Calculation of the heat flux in the lower divertor target plate using an infrared camera diagnostic system on the experimental advanced superconducting tokamak. *Nucl. Sci. Tech.* **30**, 94 (2019). <https://doi.org/10.1007/s41365-019-0625-z>
29. Y. Gao, K.F. Gan, X.Z. Gong et al., Study of striated heat flux on EAST divertor plates induced by LHW using infrared camera. *Plasma Sci. Tech.* **16**, 93 (2014). <https://doi.org/10.1088/1009-0630/16/2/02>
30. V.V. Afrosimov et al., Method of investigation of the flux of atoms emitted by a plasma. *Sov. Phys. Tech. Phys.* **5**, 1378 (1961)
31. V.I. Afanasyev, A. Gondhalekar, P.Y. Babenko et al., Neutral particle analyzer/isotope separator for measurement of hydrogen isotope composition of JET plasmas. *Rev. Sci. Instrum.* **74**, 2338 (2003). <https://doi.org/10.1063/1.1542664>
32. V.I. Afanasyev, F.V. Chernyshev, A.I. Kislyakov et al., Neutral particle analysis on ITER: present status and prospects. *Nucl.*

- Instrum. Methods Phys. Res. A **621**, 456 (2010). <https://doi.org/10.1016/j.nima.2010.06.201>
33. M.P. Petrov, V.I. Afanasyev, F.V. Chernyshev et al., 60 Years of neutral particle analysis: from early tokamaks to ITER. *Eur. Phys. J. H* **46**, 5 (2021). <https://doi.org/10.1140/epjh/s13129-021-00009-6>
  34. F.V. Chernyshev, V.I. Afanasyev, A.V. Dech et al., A compact neutral-particle analyzer for plasma diagnostics. *Instrum. Exp. Tech.* **47**, 214 (2004). <https://doi.org/10.1023/B:INET.0000025204.01783.1a>
  35. S.S. Medley, A.L. Roquemore, Construction and operation of parallel electric and magnetic field spectrometers for mass/energy resolved multi-ion charge exchange diagnostics on the Tokamak Fusion Test Reactor. *Rev. Sci. Instrum.* **69**, 2651 (1998). <https://doi.org/10.1063/1.1148994>
  36. Y.B. Zhu, A. Bortolon, W.W. Heidbrink et al., Compact solid-state neutral particle analyzer in current mode. *Rev. Sci. Instrum.* **83**, 10D304 (2012). <https://doi.org/10.1063/1.4732070>
  37. W. Li, Z.W. Xia, J. Lu et al., A new neutral particle analyzer diagnostic and its first commissioning on HL-2A. *Rev. Sci. Instrum.* **83**, 10D702 (2012). <https://doi.org/10.1063/1.4729494>
  38. W. Chen, Z.X. Wang, Energetic particles in magnetic confinement fusion plasmas. *Chin. Phys. Lett.* **37**, 125001 (2020). <https://doi.org/10.1088/0256-307x/37/12/125001>
  39. Y. Chen, W.L. Zhang, J. Bao et al., Verification of energetic-particle-induced geodesic acoustic mode in gyrokinetic particle simulations. *Chin. Phys. Lett.* **37**, 095201 (2020). <https://doi.org/10.1088/0256-307X/37/9/095201>
  40. B. Madsen, J. Huang, M. Salewski et al., Fast-ion velocity-space tomography using slowing-down regularization in EAST plasmas with co- and counter-current neutral beam injection. *Plasma Phys. Control. Fusion* **62**, 115019 (2020). <https://doi.org/10.1088/1361-6587/abb79b>
  41. S.Y. Petrov, V.I. Afanasyev, A.D. Melnik et al., Design features of the neutral particle diagnostic system for the ITER tokamak. *Phys. At. Nucl.* **80**, 1268 (2017). <https://doi.org/10.1134/S1063778817070109>
  42. M. Isobe, M. Sasao, S. Iiduka et al., Charge exchange neutral particle analysis with natural diamond detectors on LHD heliotron. *Rev. Sci. Instrum.* **72**, 611 (2001). <https://doi.org/10.1063/1.1318250>
  43. V.N. Amosov, A.V. Krasil'nikov, D.A. Skopintsev et al., A diamond-detector-based system for spectrometry of fast atoms on the JET tokamak. *Instrum. Exp. Tech.* **51**, 258 (2008). <https://doi.org/10.1134/S0020441208020188>
  44. G. Bracco, G. Betello, S. Mantovani et al., Design and calibration of the JET time of flight neutral particle analyzer with high noise rejection capability. *Rev. Sci. Instrum.* **63**, 5685 (1992). <https://doi.org/10.1063/1.1143350>
  45. D. Liu, W.W. Heidbrink, K. Tritz et al., Compact and multi-view solid state neutral particle analyzer arrays on National Spherical Torus Experiment-Upgrade. *Rev. Sci. Instrum.* **87**, 11D803 (2016). <https://doi.org/10.1063/1.4959798>
  46. J.Z. Zhang, Y.B. Zhu, J.L. Zhao et al., First results from solid state neutral particle analyzer on experimental advanced superconducting tokamak. *Rev. Sci. Instrum.* **87**, 11D834 (2016). <https://doi.org/10.1063/1.4962063>
  47. V.I. Afanasyev, M.I. Mironov, V.G. Nesenevich et al., Assessment of neutral particle analysis abilities to measure the plasma hydrogen isotope composition in ITER burning scenarios. *Plasma Phys. Control. Fusion* **55**, 045008 (2013). <https://doi.org/10.1088/0741-3335/55/4/045008>
  48. V.I. Afanasyev, F.V. Chernyshev, S.S. Kozlovsky et al., Development of the NPA based diagnostic complex in ITER. *J. Instrum.* **17**, C07001 (2022). <https://doi.org/10.1088/1748-0221/17/07/C07001>
  49. L. Ma, Y.F. Qu, Y. Luo et al., The research progress of an E//B neutral particle analyzer. *Plasma Sci. Technol.* **26**, 034002 (2024). <https://doi.org/10.1088/2058-6272/ad0c20>
  50. A.I. Kislyakov, A.V. Khudoleev, S.S. Kozlovskij et al., High energy neutral particle analyzer. *Fusion Eng. Des.* **34–35**, 107 (1997). [https://doi.org/10.1016/S0920-3796\(96\)00668-0](https://doi.org/10.1016/S0920-3796(96)00668-0)
  51. R. He, X.Y. Niu, Y. Wang et al., Advances in nuclear detection and readout techniques. *Nucl. Sci. Tech.* **34**, 205 (2023). <https://doi.org/10.1007/s41365-023-01359-0>
  52. J.L. Wiza, Microchannel plate detectors. *Nucl. Instrum. Methods* **162**, 587–601 (1979). [https://doi.org/10.1016/0029-554X\(79\)90734-1](https://doi.org/10.1016/0029-554X(79)90734-1)
  53. D.S. Bhattacharya, A. Bressan, C. Chatterjee et al., Characterization of LAPPD timing at CERN PS testbeam. *Nucl. Instrum. Methods Phys. Res. Sect. A* **1058**, 168937 (2024). <https://doi.org/10.1016/j.nima.2023.168937>
  54. J.H. Liu, Z. Ge, Q. Wang et al., Electrostatic-lenses position-sensitive TOF MCP detector for beam diagnostics and new scheme for mass measurements at HIAF. *Nucl. Sci. Tech.* **30**, 152 (2019). <https://doi.org/10.1007/s41365-019-0676-1>
  55. H.Z. Cai, Q.Y. Luo, K.X. Lin et al., Development of an ultra-fast detector and demonstration of its oscillographic application. *Nucl. Sci. Tech.* **33**, 72 (2022). <https://doi.org/10.1007/s41365-022-01055-5>
  56. M. Krems, J. Zirbel, M. Thomason et al., Channel electron multiplier and channelplate efficiencies for detecting positive ions. *Rev. Sci. Instrum.* **76**, 093305 (2005). <https://doi.org/10.1063/1.2052052>
  57. H.Y. Zhu, J.L. Lou, Y.L. Ye et al., Two annular CsI(Tl) detector arrays for the charged particle telescopes. *Nucl. Sci. Tech.* **34**, 159 (2023). <https://doi.org/10.1007/s41365-023-01319-8>
  58. X.C. Han, S. Wang, H.Y. Wu et al., CsI-bowl: an ancillary detector for exit channel selection in  $\gamma$ -ray spectroscopy experiments. *Nucl. Sci. Tech.* **34**, 133 (2023). <https://doi.org/10.1007/s41365-023-01289-x>
  59. Y. Luo, L. Ma, D.H. Xie et al., Characterization of the energy response of a LYSO+SiPM detector module for E//B NPA using  $\alpha$  and hydrogen ions. *Nucl. Instrum. Methods Phys. Res. A* **1061**, 169110 (2024). <https://doi.org/10.1016/j.nima.2024.169110>
  60. D.W. Cooke, K.J. McClellan, B.L. Bennett et al., Crystal growth and optical characterization of cerium-doped  $\text{Lu}_{1.8}\text{Y}_{0.2}\text{SiO}_5$ . *J. Appl. Phys.* **88**, 7360 (2000). <https://doi.org/10.1063/1.1328775>
  61. U.F. Ahmad, Y.S. Wudil, A. Imam et al., Applications of carbon-based diamond detectors: a critical review. *Mater. Today Commun.* **36**, 106409 (2023). <https://doi.org/10.1016/j.mtcomm.2023.106409>
  62. A.V. Krasilnikov, E.A. Azizov, A.L. Roquemore et al., TFTR natural diamond detectors based D-T neutron spectrometry system. *Rev. Sci. Instrum.* **68**, 553 (1997). <https://doi.org/10.1063/1.1147651>
  63. L.G. Zang, Y.F. Qu, W.P. Lin et al., Design of the electromagnetic field for an E//B neutral particle analyzer. *Plasma Fusion Res.* **15**, 2402036 (2020). <https://doi.org/10.1585/pfr.15.2402036>
  64. Y. Luo, W.P. Lin, P.P. Ren et al., A simulation study of a windowless gas-stripping room in an E//B neutral particle analyzer. *Nucl. Sci. Tech.* **32**, 69 (2021). <https://doi.org/10.1007/s41365-021-00909-8>
  65. ANSYS Fluent. <https://www.ansys.com>
  66. B. Mohamedi, S. Hanini, A. Ararem et al., Simulation of nucleate boiling under ANSYS-FLUENT code by using RPI model coupling with artificial neural networks. *Nucl. Sci. Tech.* **26**, 040601 (2015). <https://doi.org/10.13538/j.1001-8042/nst.26.040601>
  67. M. Ady, R. Kersevan, Introduction to the latest version of the test-particle Monte Carlo code molflow+, in *Proceeding of the 10th Int. Particle Accelerator Conf.*, Dresden, Germany, (June

- 2014), pp. 2348–2350. <https://doi.org/10.18429/JACoW-IPAC2019-TUPMP037>
68. S. Agostinelli, J. Allison, K. Amako et al., Geant4-a simulation toolkit. *Nucl. Instrum. Methods Phys. Res. A* **506**, 250 (2003). [https://doi.org/10.1016/S0168-9002\(03\)01368-8](https://doi.org/10.1016/S0168-9002(03)01368-8)
69. J. Allison, K. Amako, J. Apostolakis et al., Recent developments in Geant4. *Nucl. Instrum. Methods Phys. Res. A* **835**, 186 (2016). <https://doi.org/10.1016/j.nima.2016.06.125>
70. L.G. Zang, Y.F. Qu, Y. Luo et al., Design of the stripping unit and the electromagnetic analysis unit for the E//B NPA on HL-2A/2M tokamak. *Plasma Sci. Technol* **24**, 064002 (2022). <https://doi.org/10.1088/2058-6272/ac6090>
71. H.T. Hunter, M.I. Kirkpatrick, I. Alvarez et al., Atomic data for fusion, ORNL-6086/V1. United States (1990). <https://doi.org/10.2172/6570226>
72. Y..G. Liu, J..L. Liu, Q. Wu et al., Ion beam production with an antenna type 2.45 GHz electron cyclotron resonance ion source. *Rev. Sci. Instrum.* **91**, 023301 (2020). <https://doi.org/10.1063/1.5128393>
73. W..B. Wu, H..T. Ren, S..X. Peng et al., Understanding hydrogen plasma processes based on the diagnostic results of 2.45 GHz ECRIS at Peking University. *Chin. Phys. B* **26**, 095204 (2017). <https://doi.org/10.1088/1674-1056/26/9/095204>
74. W.B. Wu, A.L. Zhang, S.X. Peng et al., A global model of 2.45 GHz ECR ion sources for high intensity  $H^+$ ,  $H^{2+}$  and  $H^{3+}$  beams. *Vacuum* **182**, 109744 (2020). <https://doi.org/10.1016/j.vacuum.2020.109744>
75. S.X. Peng, W.B. Wu, H.T. Ren et al., Possibility of generating  $H^+$ , or  $H^{2+}$ , or  $H^{3+}$  dominated ion beams with a 2.45 GHz permanent magnet ECR ion source. *Rev. Sci. Instrum.* **90**, 123305 (2019). <https://doi.org/10.1063/1.5128019>

Springer Nature or its licensor (e.g. a society or other partner) holds exclusive rights to this article under a publishing agreement with the author(s) or other rightsholder(s); author self-archiving of the accepted manuscript version of this article is solely governed by the terms of such publishing agreement and applicable law.